Phase diagram for nanodroplet impact on solid spheres：From hydrophilic to superhydrophobic surfaces

Mingjun Liao (廖明俊),[a] Qianyi Liu (刘钱艺),[a] Zhiyin Yang,[b] Amirali Shateri,[b] Wenpeng Hong (洪文鹏),[a] and Fangfang Xie (解芳芳)[a, *]

[a] School of Energy and Power Engineering, Northeast Electric Power University, Jilin, 132012,

China

[b] School of Engineering, University of Derby, DE22 3AW, United Kingdom

[*]**Corresponding Author:** xiefang705@163.com;

ABSTRACT: The impact of droplets on solid surfaces is a crucial fluid phenomenon in additive industry, biotechnology, and chemistry, where controlling impact dynamics and duration is essential. While extensive research has focused on flat substrates, our understanding of impact dynamics on curved surfaces remains limited. This study seeks to establish phase diagrams for the process of droplet impact on solid spheres and further quantitatively describe the effect of curvature through theoretical analysis. It aims to determine the critical conditions between different impact outcomes and also establish a scaling relationship for the contact time. Here, the post impact outcome regimes occurring for a wide range of Weber numbers (We) from 1.2 to 173.8, diameter ratio (λ) of solid spheres to nanodropets from 0.25 to 2, and surface wettability (θ) from 21° to 160°, through the molecular dynamics simulation method (MD) and theoretical analysis. The MD simulations reveal that the phase diagrams of droplet impacts on hydrophilic, hydrophobic, and superhydrophobic spheres differ, with specific distinctions focusing on rebound and three different forms of dripping. Furthermore, a theoretical model based on the principle of energy conservation during impact on superhydrophobic surfaces has been developed to predict the critical conditions between rebound and dripping states, showing good agreement with simulation results. Additionally, a new scaling relationship of contact time for droplet impact on superhydrophobic spherical surfaces has also been established by extending and modifying the existing models, which also agrees well with the simulated results. These insights provide a foundational understanding for designing surface structures.

I. INTRODUCTION：

The impact of a droplet on a solid sphere is a complex fluid dynamics phenomenon involving multiple variables such as impact velocity, surface wettability, and sphere size. This is a ubiquitous

phenomenon in various industries, biotechnology, chemistry, and pharmaceuticals, such as in painting,[1] spray cooling,[2] coating,[3] 3D printing[4] and drug delivery[5] etc. By studying the impact of droplets on spheres, one can better understand and control the critical factors in these application processes. For instance, in cold weather, when the raindrops collide with power transmission lines,[6] it is highly likely to freeze on the curved surface, accelerating the rebound of the droplets after impacting, and reducing contact time will help achieve anti-icing. In the procedure of spray drying,[7] the coating agent sprayed on the particles needs to be transformed from a fluid state to dry particles, promoting the sprayed droplets spreading will help to form a good spinning effect. In the Fluid Catalytic Cracking (FCC) industry,[8] atomized droplets of heavy fuel collide with hot solid catalyst particles in the FCC reactor. The breakdown of long-chain molecules occurs at the interface between the liquid and solid, thereby enhancing the industrial value of the heavy fuel. The results of these droplet-particle collisions play a critical role in determining the ultimate quality of the products. In the applications mentioned above, interactions between droplets and spheres play a role in heat and mass transfer, impacting the quality of final products. Consequently, ongoing investigation into droplet-sphere collisions can enhance our knowledge of liquid bridges, spherical agglomeration, and the behavior of wet spheres. This understanding is valuable for modeling and designing industrial reactors.

Recent studies of the droplet impact on spherical surfaces, encompassing both experiments and simulations, have been conducted due to the wide range of applications in this field. Banitabaei et al.[9] investigated the process of droplet impact on a stationary sphere through experimental methods. Their focus was on the effects of impact velocity and the wettability of the sphere's surface on the collision outcomes. The study extended the Weber number range significantly, from 0.1 to 1146. It

was observed that higher-speed droplets impacting a hydrophobic sphere formed a thin liquid film, known as a lamella. During the experiment, various geometric parameters of the droplet impact were measured, including the length of the lamella and the diameter of its base. Li et al.[10] examined the dynamics of droplet impact on solid spheres, focusing on the effects of surface wettability, sphere size, and initial impact velocity. The results showed that at lower impact velocities, the droplet tends to retain a hemispherical shape; while at higher velocities, the droplet on smaller spheres may completely envelop the sphere or even drip off. Du et al.[11] further explored the influence of fluid properties and sphere diameter during droplet impact on spherical surfaces. The study found that the maximum spreading factor of the droplet is related to the fluid's Reynolds and Weber numbers, suggesting these results could be used to optimize industrial painting and coating processes. Xia et al.[12] investigated the dynamics of droplet impact on superhydrophobic spheres, particularly the impact of protrusions on impact dynamics. The research revealed various dynamic behaviors, such as contactless bouncing, conventional bouncing, and ring-shaped bouncing. Liu et al.[13] focused on the rebound and dripping behavior of droplets on small superhydrophobic spheres, particularly examining how Weber number and sphere-to-droplet diameter ratio affect impact dynamics. Li et al.[14] used the many-body dissipative particle dynamics (MDPD) method to investigate droplet impacts on superhydrophobic solid spheres of various sizes. The results indicated that the impact velocity and sphere size affect the post-impact shape of the droplet, with four distinct spreading types observed: bouncing, wrapping, dripping, and a combination of bouncing and dripping. Dalgamoni et al.[15] combined the axisymmetric lattice Boltzmann method (LBM) with theoretical analysis to study the dynamics of droplet impacts on spherical surfaces, focusing on the effects of Weber number, sphere radius, and surface wettability. The study revealed

4

five distinct impact outcomes and established a simulation-predicted phase diagram to illustrate the different collision results.

With advancements in technology and precision instruments, applications in some microscale domains are increasingly involving nanodroplet impacts. Some examples of these applications include high-throughput biological screening,[16] using phase-change nanodroplets to treat cancer,[17] and the preparation of high-entropy metallic glass nanoparticles.[18] As a result, nanodroplet impact has become an important topic closely related to production and daily life. However, experiments at this scale are impractical and can only be supplemented by numerical simulations. Molecular dynamics (MD) simulation is a reliable tool for addressing these challenges. Additionally, recent studies have revealed scale effects between the nanoscale and the macroscale on two levels, indicating that the results and parameters for droplet impact at the macroscale are different from those at the nanoscale. The specific reasons are as follows: first, at the nanoscale, the influence of surface tension and intermolecular forces becomes more pronounced, factors that are typically not considered in macroscopic models. At this scale, surface effects dominate because the surface area-to-volume ratio of nanoscale droplets increases significantly, leading surface tension to play a crucial role in the dynamics. Additionally, the traditional continuum assumption presumes that matter is continuous, which is reasonable at the macroscopic scale. However, at the nanoscale, due to the impact of molecular discreteness, this assumption no longer holds. The collision and spreading behavior of nanoscale droplets is significantly influenced by interactions between individual molecules or atoms, resulting in dynamics that differ from those at the macroscopic scale. Consequently, the macroscopic scaling laws based on the continuum assumption fail at the nanoscale, making them inaccurate for predicting system behavior. For example, at the macroscale,

the no-slip boundary condition is used in continuum-level models to simplify the treatment of the

interaction between droplets and surfaces.[19-21] However, at the nanoscale, the no-slip boundary

condition no longer applies, as significant slip is observed for nanodoplet flowing on a solid

plate.[22-24] Second, at the nanoscale, the effect of viscous forces becomes more prominent. For

example, at the macroscale, in the context of droplet rebound after impact, the contact time is

proportional to the Weber number ($We=(\rho R_0 v_0^2)/\gamma$) across a wide range of We, expressed by

$\tau_0 \sim (\rho R_0^3/\gamma)^{1/2}=(R_0/v_0)We^{1/2}$, where ρ is the density, γ is the surface tension, R_0 is the droplet radius, v_0

is the impact velocity.[25-31] However, at the nanoscale, at higher Weber numbers, the contact time

becomes proportional to both the We and the Reynolds number ($Re=\rho v_0 R_0/\mu$), expressed by

$\tau \sim (\rho \mu R_0^4/\gamma^2)^{1/3}=(R_0/v_0)We^{2/3}Re^{-1/3}$, where μ is the liquid viscosity.[32] Physically, Weber number is the

ratio of inertial to surface tension forces, while the Reynolds number is the ratio of inertial to

viscous forces. Thus, the difference in scaling relationships for contact time between the two scales

indicates that, at the macroscale, the droplet rebound process is governed only by inertial forces,

represented by We, while at the nanoscale, it is influenced by both inertial and viscous forces,

represented by We and Re. Similarly, studies on the maximum spreading factor ($\beta_{max}=D_{max}/D_0$,

where D_{max} is the maximum spreading diameter, D_0 is the droplet diameter) have also shown a

different scaling relationship at different scales. At the macroscale, β_{max} scales as $We^{1/4}$,[33] but at the

nanoscale, with higher Weber numbers, $\beta_{max} \sim We^{1/2}Oh^{1/3}$ ($Oh=\mu/(\rho D_0 \gamma)^{1/2}$, representing the ratio of

viscous to inertial-capillary forces),[34] which also proves that when the size of the droplet is reduced

to the nanoscale, viscous forces become an important influencing factor. This can be inferred from

the relative magnitude of the Oh at the two scales. For example, in the case of water droplets, the

Oh is only about O (10^{-3}) at the macroscale but can increase to about O (1) when the droplet

diameter is reduced to the nanoscale, which means that the proportion of viscous forces has increased significantly. The fundamental reason for the prominent effect of viscous forces at the nanoscale lies in the change in the internal velocity distribution during droplet impact between the two scales. Since Newton's law of viscosity states that the magnitude of viscous force is directly proportional to the velocity gradient, different velocity distributions directly lead to different magnitudes of viscous forces. At the macroscale, the velocity gradient only appears in the boundary layer,[35-44] making the viscous force comparatively negligible against other forces. However, at the nanoscale, the velocity gradient is distributed throughout the entire droplet,[45] making viscous forces significant and a crucial factor in droplet impact dynamics. Thus, the existence of scale effects means that conclusions derived at the macroscale are no longer applicable at the nanoscale, necessitating further study through nanoscale numerical simulations. Molecular dynamics simulations have successfully addressed this challenge.

Nonetheless, there are currently only three papers on nanodroplet impacts on spheres. Among them, Yin et al.[46] explored the behavior of individual water nanodroplets vertically impacting a curved copper substrate, investigating the effects of impact velocity, potential energy depth between oxygen and copper atoms, and substrate curvature. The research indicated that higher-velocity impacts might lead to splashing, while droplets at lower velocities exhibited a process of spreading and contraction. Zhan et al.[47] used MD simulations to investigate the dynamic processes of droplet-particle collisions, examining various influencing factors including the Weber number, equilibrium contact angle, and the ratio of sphere to droplet size. The study revealed two distinct rupture modes and presented collision outcome maps based on these factors. The latest paper by Wang et al.[48] aimed to reported the outcome regimes of nanodroplets impacting on hydrophobic

solid spheres and to revealed the curvature effect across a wide range of conditions, including different Weber numbers, diameter ratios between nanodroplets and solid spheres, and contact angles. Although these studies have covered certain aspects of the dynamic process and outcomes of nanodroplet impacts on solid spheres, a complete phase diagram has yet to be established. This phase diagram should encompass the wettability range of the sphere, from hydrophilic to superhydrophobic, the radius ratio between the sphere and droplet (λ), from much smaller than 1 to much larger than 1, and a sufficiently large range of impact velocities. The phase diagram is designed to predict the different outcomes of droplet impacts on specific surfaces by analyzing key influencing factors. A comprehensive phase diagram is crucial for surface design in certain applications where droplet impacts play a role. As mentioned earlier, results at the nanoscale can differ significantly from those at the macroscale, and current research at the nanoscale is sparse. Therefore, creating a nanoscale phase diagram is critical. Furthermore, quantitatively predicting different impact outcomes using theoretical formulas has not yet been sufficiently established. Furthermore, the variation patterns and scaling relationships of contact time, a crucial parameter, have not been reported in the literatures,[46-48] indicating a need for further in-depth research.

This study aims to develop a comprehensive phase diagram that illustrates various outcomes of nanodroplet impacts and to establish theoretical formulas to predict the critical conditions for different impact outcomes and the variation of contact time. The analysis spans a range of λ values between 0.25 and 2 and *We* between 1.2 and 173.8. Additionally, different surface wettabilities, with contact angles (θ) ranging from 21 to 160 degrees, are taken into account. The study will be divided into three parts, namely the impact of nanodroplets on hydrophilic, hydrophobic, and superhydrophobic spheres. Subsequently, corresponding phase diagrams will be organized based on

the impact results on surfaces with different wettability, detailing the unique dynamic behaviors for each outcome utilizing snapshots obtained from MD simulations. It will then focus on the theoretical analyses of establishing transition criteria and contact times for droplet impacts on superhydrophobic surfaces.

II. MODEL AND METHOD

Molecular dynamics simulations are utilized to study the behavior of nanodroplets when they collide with solid spheres. These simulations are carried out using the LAMMPS software package, designed for large-scale atomic and molecular simulations. The equations of atomic motion are solved using the velocity-Verlet algorithm. The computational setup includes a solid platinum sphere with variable diameters (D_s) from 2 nm to 16 nm and a spherical water droplet with a fixed diameter of 8 nm (D_0), which are placed in a simulation box of 80 nm × 80 nm ×80 nm, depicted in Figure 1. The solid platinum sphere and liquid water droplet are both modeled by face-centered cubic (FCC) with a lattice constant of 0.39 nm and 0.49 nm, distinctively. In the simulation, the solid platinum sphere is always placed on the center of the box, and the distance between the bottom of the droplet and the top of the sphere is 2 nm. Moreover, to prevent the solid sphere from deforming or disintegrating during droplet impact, a virtual spring force is added between the atoms within the sphere. It should be mentioned that the water description employs the mW (monatomic water) model, a coarse-grained approach introduced by Molinero and Moore,[49] which has been widely used in MD studies of droplet-wall impacts.[34,45,48,50] This is not only because coarse-grained models are computationally efficient, resulting in significant cost savings, but also because, even with its structural simplifications, this model accurately replicates key characteristics of water, such as density, surface tension, and viscosity. However, a caveat is that the absence of hydrogen atom

reorientation leads to a viscosity that is three times lower than the experimental value. According to Li et al.[45] the properties of mW water are ρ=996 kg m^{-3}, μ=283.7μPa s, and γ=66 mN m^{-1}. It is worth noting that the droplet parameters here differ from those at the macroscopic scale. This is because materials exhibit unique properties at the nanoscale that are different from those at the macroscopic scale. Specifically, the enhanced surface interactions and the discreteness of matter at the nanoscale have a significant impact on simulation results. Traditional macroscopic models often overlook these nanoscale characteristics, so adjusted parameters are used in MD simulations to more accurately capture these phenomena.
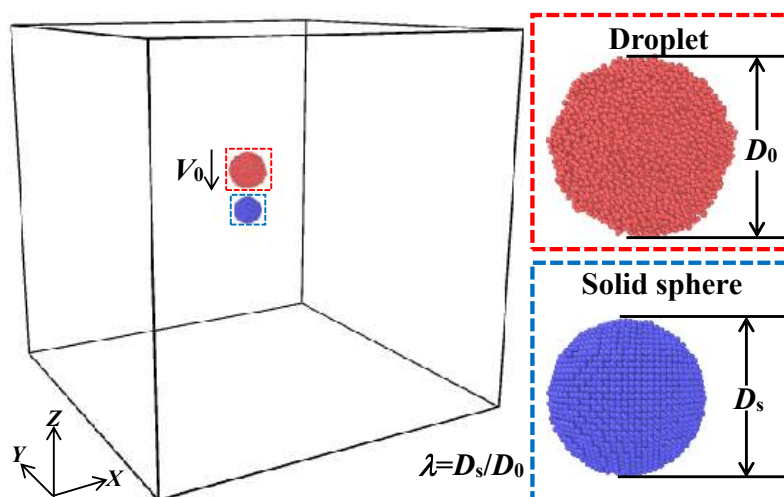

Fig. 1. Schematic diagram of three-dimensional computation domains for droplet-sphere collision system, where the red dashed box contains a droplet with a diameter of D_0, while the blue dashed box contains a solid sphere with a diameter of D_s. The diameter ratio is defined as $\lambda=D_s/D_0$, and the velocity applied during the impact is V_0.

The Lennard-Jones 12-6 potentials are employed to simulate the interaction of solid-solid (s-s) and solid-liquid (s-l), expressed as

1

$$U(r) = 4\varepsilon\left[\left(\sigma/r\right)^{12} - \left(\sigma/r\right)^{6}\right] \tag{1}$$

where r represents the distance between two atoms, ε is the depth of the potential well, and σ is the distance at which the potential crosses zero. If the distance between two atoms is sufficiently large, the potential value approaches zero, indicating negligible interactions. To reduce computational costs from such negligible interactions, a cutoff distance, r_{cut}=1 nm, is used.[45] The interaction potential in the above formula is calculated only when $r < r_{cut}$. Based on earlier studies of nanodroplet impacts on solid surfaces, the constant parameters are $\sigma_{s\text{-}s}$ = 2.47 Å, $\sigma_{s\text{-}l}$ = 2.82 Å, $\varepsilon_{s\text{-}s}$ = 0.69 eV, and another adjustable parameter $\varepsilon_{s\text{-}l}$, which is used to modify the wettability of solid surfaces scales from 0.0236 eV (21°) to 0.0027 eV (160°).[51]

After designing the initial simulation system and the interatomic interaction force field, the first step is to perform energy minimization. This is achieved by adjusting the molecular structure to lower the system's potential energy, ensuring that the force field parameters are appropriately applied to the system, resulting in more accurate simulation outcomes. This brings the system to a stable state, providing a reasonable starting point for subsequent simulations and calculations, while also reducing convergence time. This is a crucial step in the MD simulations, providing a reliable foundation for further simulations. The next step is to simulate the equilibrium state of the entire system. The so-called equilibrium phase involves bringing the system into an NVT ensemble (canonical ensemble) for 3 nanoseconds, during which a Nose-Hoover thermostat maintains the system's temperature at 300 K. Subsequently, the system will be switched to an NVE ensemble (microcanonical ensemble) for 2 nanoseconds, where the heat bath will be removed. The purpose of running under this ensemble is to enable the atoms within the system to achieve a balanced state without external energy input. Throughout the entire equilibrium stage, the centers of the

1

nanodroplet and the solid sphere are fixed in their initial positions to prevent any interactions between them. Once equilibrium is reached, indicated by stable energy, temperature, and pressure levels, the simulation transitions to the next stage: the output stage. In this final output stage, the system will be simulated under the NVE ensemble, and the command to fix the nanodroplet's center of mass will be replaced with the application of a downward velocity (V_0), thus facilitating the collision process between the droplet and the sphere. This will also lead to different collision outcomes based on the applied velocity. This stage must run for 0.3 ns to ensure complete output of results under all conditions. For analysis, the position and velocity of each atom are recorded every 1 picosecond to track the dynamics of the system throughout the simulation. Periodic boundary conditions are specified in the X and Y directions, whereas a reflecting wall is employed in the Z direction. The coordinates of atoms are output every 1000 steps. Simulation results are analyzed by the Ovito (Open Visualization Tool) software.[51] During the numerical simulations, we observed instances of asymmetry in the droplet shape. This is primarily attributed to the inherent randomness and limitations of the MD method, where the irregular motion of molecules, coupled with the reduced time scales involved, may lead to momentary asymmetry. However, such asymmetry does not significantly impact the overall outcomes, as the droplet may regain symmetry over time, and the essential parameters such as temperature, pressure, and energy stabilize during the simulation. To further ensure the robustness of our results, repeated calculations were performed under varying conditions, which confirmed the reliability of our findings.

To validate the reliability of our MD code, a series of simulations of nanodroplet impacts on solid surfaces were conducted and the results were compared with those from existing literature. Specifically, the same initial conditions as Li et al.[52] were used, including droplet diameter, contact

angle, and impact velocity. By comparing the temporal evolution of droplet spreading diameter, it was found that the current simulation results were in excellent agreement with those of Li et al,[52] as shown in Fig. 2. This comparison demonstrates the high accuracy and reliability of our MD simulation method. Similar validation processes can also be found in our previous works.[32,53]
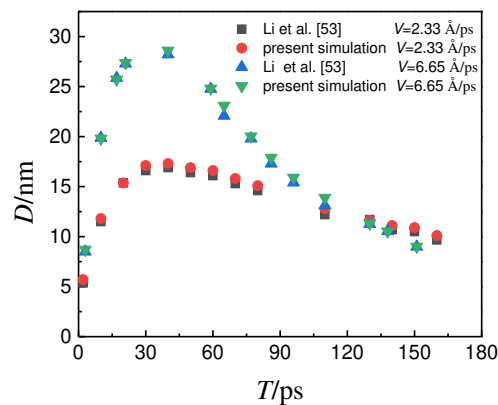

Fig. 2. Comparison of temporal evolution of spreading diameter from the present simulation and the previous study.[52] Droplet diameter D_0=13.2 nm, contact angle θ=125°, and impacting velocity V_0=2.33 and 6.65 Å/ps.

III. RESULTS AND DISCUSSION

Based on previous studies, it can be concluded that wall wettability, droplet impact velocity, and the diameter ratio between the droplet and the sphere are the three key factors affecting the outcome of droplet-sphere impacts.[10,15,46-48] Creating a three-dimensional phase diagram built on these three parameters not only makes the chart overly complex, with excessive information and difficulty in extracting key insights, but also increases the level of difficulty in understanding, preventing a clear visualization of the relationships between the variables. Therefore, in this study,

1

we extract wall wettability as an individual variable, dividing it into hydrophilic, hydrophobic, and superhydrophobic regions. Within each of these regions, a two-dimensional phase diagram using droplet impact velocity and diameter ratio is constructed, aiming to present the findings in a clearer and more comprehensible manner. It should be noted that to increase the diagram's general applicability, the dimensional impact velocity is replaced with the dimensionless Weber number, as is commonly done in most papers.[10-15,46-48]

A. Impact on hydrophilic sphere

The hydrophilic region was analyzed using contact angles of 21°, 55°, and 75°. The impact results for these three hydrophilic angles were found to be consistent. Specifically, as the impact velocity increased, the outcomes sequentially exhibited deposition, covering, ligament-structured dripping (dripping 1), and conical-structured dripping (dripping 2) when $\lambda \leq 1$. Here, four sets of snapshots are provided as examples at θ=55°, λ=0.75, and We=4.83, 59.16, 120.73, 173.85 to illustrate the four outcomes, as shown in Fig. 3. Fig. 3 (a) illustrates the process of the outcome of deposition when We=4.83. The moment when the droplet contacts the spherical surface is defined as time 0. Due to the inertia, the droplet spreads along the spherical surface after contacting it. Furthermore, due to the hydrophilic nature of the surface, the adhesion force between the droplet and the sphere is significant. As a result, the droplet quickly spreads on the sphere surface, forming a wrapping liquid film, as shown in the snapshot at t=45 ps. However, due to the significant adhesion work and viscous dissipation during spreading, the droplet has no excess surface energy and kinetic energy after reaching its maximum spreading state, stabilizing on the sphere surface in the form of a liquid film.

As the impact velocity increases, at We=59.16, due to the increase in kinetic energy, the droplet

1

continues to spread on both sides of the sphere until it overlaps at the bottom, forming a complete liquid film, achieving full coverage of the sphere, thus forming the covering state (Fig. 3b). If the impact velocity continues to increase, at We=120.73, after covering the sphere, the droplet still has residual kinetic energy, causing it to continue moving downward. However, due to the strong wetting, the part of the liquid film close to the sphere remains attached to the surface. This leads to the continuous elongation and thinning of the lower end of the droplet, forming a spindle shape. Eventually, the droplet undergoes a breakage process at the narrowest point of the liquid film. As a result, a portion of the droplet remains attached to the spherical surface in the form of a liquid film, while the remaining part of the droplet detaches from the sphere and moves downward. This state is referred to as dripping 1 (Fig. 3c). Another newly identified type, dripping 2 (Fig. 3d), differs significantly from dripping 1. After reaching the maximum spreading state represented at t=9 ps, the liquid film does not cover the sphere but instead moves downward as a whole in a conical shape. Thus, at t=17 ps, most of the liquid separates from the sphere in a conical structure, leaving only a few droplets attached to the sphere. The fundamental reason for these two different forms of dripping is whether the provided kinetic energy can overcome the adhesion work generated by the hydrophilic surface, allowing the droplet to move downward without adhering laterally to the sphere. Similar conclusions have also been found and reported in.[47,54]

It should be noted that at θ=75°, a special state occurs as long as $\lambda \leqslant 1$, namely the deposition of a droplet at the bottom of the sphere. Taking λ=0.5 and We=30.18 as an example, the impact process is shown in Fig. 4. It is found that when $t \leqslant 60$ ps, the development process of the droplet is similar to that of $t \leqslant 55$ ps in Fig. 3b. However, in this process, as the wetting property weakens, the adhesion work generated by the relative motion between the droplet and the sphere decreases. This

1

allows the droplet to retain residual kinetic energy after completely wrapping the sphere, resulting in the rupture of the liquid film at the top of the sphere at t=100 ps. The droplet then continues to move downward along the sides of the sphere. However, its remaining kinetic energy is not sufficient to detach it from the sphere, thus ultimately forming a special deposition form at the bottom of the sphere.
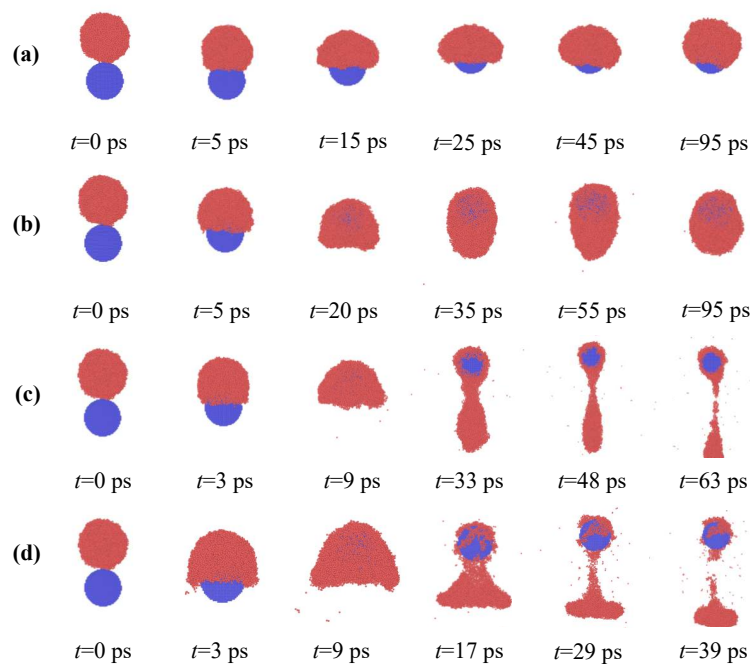

Fig. 3. Temporal evolutions of droplet profiles on the sphere at θ=55° and λ=0.75 at We = (a) 4.83, (b) 59.16, (c) 120.73, and (d) 173.85.
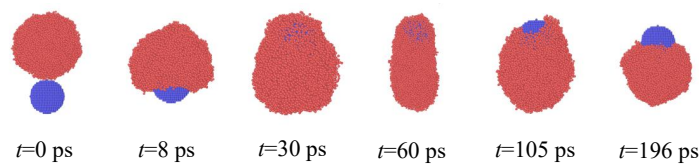

Fig. 4. Temporal evolutions of droplet profiles on the sphere at θ=75°, λ=0. 5 and We=30.18.

1

When λ>1, the impact outcomes differ significantly from those when λ≤1. At this region, only two outcomes occur: deposition and splash. Specifically, when the sphere diameter is greater than the droplet diameter, the impact results resemble those of a droplet impacting a flat surface.[52,55] These two outcomes also occur only under hydrophilic conditions. Taking θ=75°, λ=2, We=97.79, and We=173.85 as examples, two sets of snapshots are provided to illustrate the two outcomes, as shown in Fig. 5. Due to the increase in sphere radius, when the droplet reaches its maximum spreading extent, it can only be located at the upper part of the solid sphere's center (at t=20 ps in Fig. 5a). Subsequently, it begins to contract and eventually stabilizes by depositing at the top of the sphere.
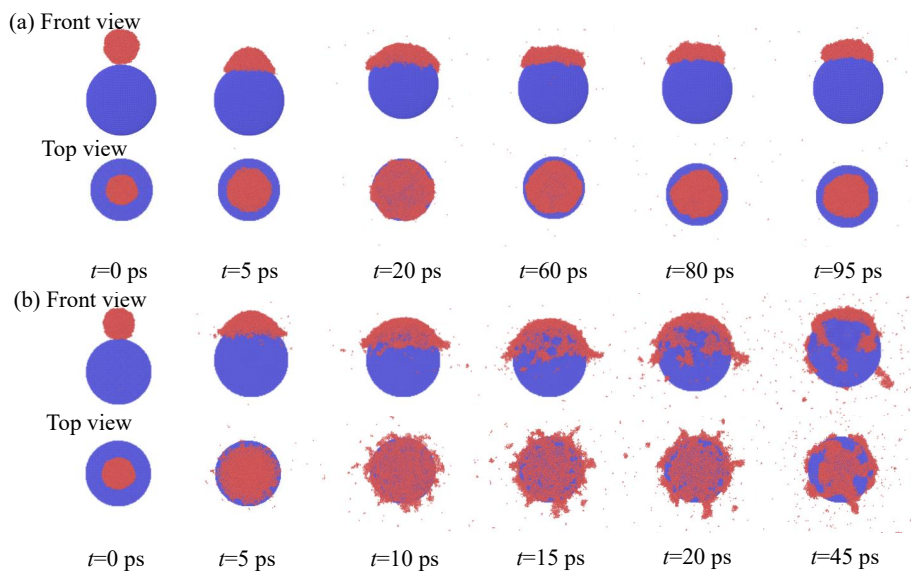

Fig. 5. Temporal evolutions of droplet profiles on the sphere ath θ=75° and λ=2 at We = (a) 97.79, (b) 173.85.

If the impact velocity continues to increase, the strong adhesive effect of the hydrophilic

1

surface on the liquid will cause the liquid film to promote splash (Fig. 5b). The splash emerges along the perimeter of the extending liquid layer. In a macroscopic study by Bischofberger et al.[56], a comparable splash phenomenon was observed when a low-viscosity water-ethanol droplet at a macroscale impacted a smooth glass surface, resulting in numerous small daughter droplets ejecting above the lamella. In another MD simulation by Ma et al.[50], it was also been observed that when nanoscale droplets impacted a hydrophilic surface with a contact angle of 33 degrees, this phenomenon of initial edge fragmentation occurred. Wang et al.[57] recently discussed the distinct difference and underlying mechanism behind the splash phenomenon at these two scales. They proposed that while the immediate splash of macroscale droplets is triggered by air bubbles beneath the extending lamella, the Rayleigh-Taylor instability of ejected rims, induced by the rapidly decelerating extending lamella, leads to the immediate splash of nanodroplets.

While the contact angle is an important factor influencing droplet impact behavior, within the parameter range of this study, it is found that the trend of the phase diagrams is consistent across different contact angles, with only slight differences at the critical points. Hence, the phase diagram for the $55°$ contact angle based on the variations of the impact results with λ and We is shown in Fig. 6 can be considered representative of the behavior at other contact angles, such as $21°$ and $75°$. In this figure, deposition is marked by black squares, covering by red triangles, dripping 1 by blue triangles, dripping 2 by pink triangles, and splash by green diamonds. It can be clearly seen that five types of impact results appear in the hydrophilic region. It was found that when $0.5 \leq \lambda \leq 1$, the results of droplet impact on the spherical surface showed four outcomes with increasing impact velocity: deposition, covering, dripping 1, and dripping 2. However, at $\lambda=0.25$, the first outcome of deposition was missing. Even if the impact velocity is very small, the droplet will achieve complete

1

covering status because the droplet radius is much larger than the sphere radius. As long as the droplet contacts the sphere under the action of small velocity, it will continue to move downward under the action of inertia and viscosity until it completely covers the entire sphere. With the increase in sphere diameter, that is, an increase in λ, this small inertia force is not enough to keep the droplet moving downward. When its kinetic energy is consumed completely, the droplet cannot achieve complete coverage of the sphere. Therefore, under low velocity conditions, the state is stabilized on the solid sphere as deposition.

It is also observed that when $\lambda \leq 0.5$, the dripping state occupies a large proportion. However, when $\lambda > 0.5$, the proportion of deposition state gradually increases. When $\lambda > 1$, splash only occurs when We reaches 150, while deposition state occurs under all other velocity conditions. Moreover, it can be concluded that in the hydrophilic region, $\lambda = 1$ can be considered as the dividing line for categorizing impact results into a complex region with smaller λ ($\lambda \leq 1$) and a relatively simple region similar to droplet impacting a flat surface with larger λ ($\lambda > 1$). Additionally, the dripping state only appears when $\lambda \leq 1$, while splash only occurs when $\lambda > 1$. It is important to note that in the case of macroscopic droplet impact on hydrophilic spheres, it typically results in deposition or covering. For example, the experimental results by Rioboo et al.[58] show that at lower We, the droplet spreads on the hydrophilic surface and eventually stabilizes into a deposition state. However, our MD simulations show that at the nanoscale, droplets under the same conditions may exhibit different behaviors. For instance, at higher We, droplets may undergo significant deformation and might display partial dripping or splash phenomena, contrasting with the predominant deposition behavior observed at the macroscopic scale. This discrepancy may arise from the complex interplay between surface energy and droplet dynamics at the nanoscale.
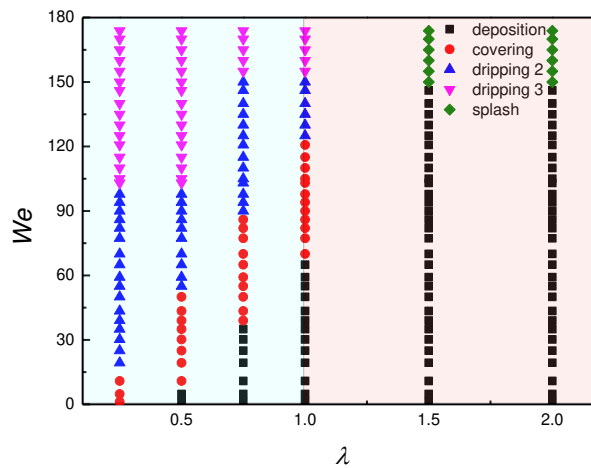
1

Fig. 6. Phase diagram of nanodroplet impact on a hydrophilic sphere, where We ranges from 1.21 to 173.84 and λ ranges from 0.25 to 2.

B. Impact on hydrophobic sphere

In the hydrophobic region, we conducted comparative studies on the impact results of nanodroplets at contact angles of 105°, 125°, and 135°. The results differ from those in the hydrophilic region. In this region, under any diameter ratio condition, the rebound state occurs, and the dripping 1 state no longer appears. Instead, a new state, dripping 3, emerges. The results at the three contact angles are also similar, with slight differences in the critical points between adjacent outcomes, as observed in the hydrophilic region.

Here, taking θ=125°, λ=1, and We=1.21,19.32,59.16,146.08 as examples to illustrate four states: deposition, rebound, dripping 2, and dripping 3, as shown in Fig. 7. When the droplet impacts the sphere at a very low velocity, the provided kinetic energy is insufficient to overcome viscous dissipation. Consequently, the droplet attaches to the hydrophobic spherical surface with a small

2

contact angle, forming the deposition state (Fig. 7a). However, by slightly increasing the impact velocity, the droplet exhibits an outcome of rebound (Fig. 7b). During this process, it is observed that due to the enhanced hydrophobicity of the surface, the droplet no longer spreads completely along both sides of the sphere, as shown in Fig. 3, but instead, the internal liquid close to the sphere surface spreads along the sphere while a portion of the external liquid spreads laterally. This forms a crown-like shape, similar to impacting on an invisible flat surface, thereby reducing the viscous dissipation generated by the droplet's contact with the sphere. As a result, more residual kinetic energy is accumulated, causing the droplet to contract and bounce off the spherical surface.
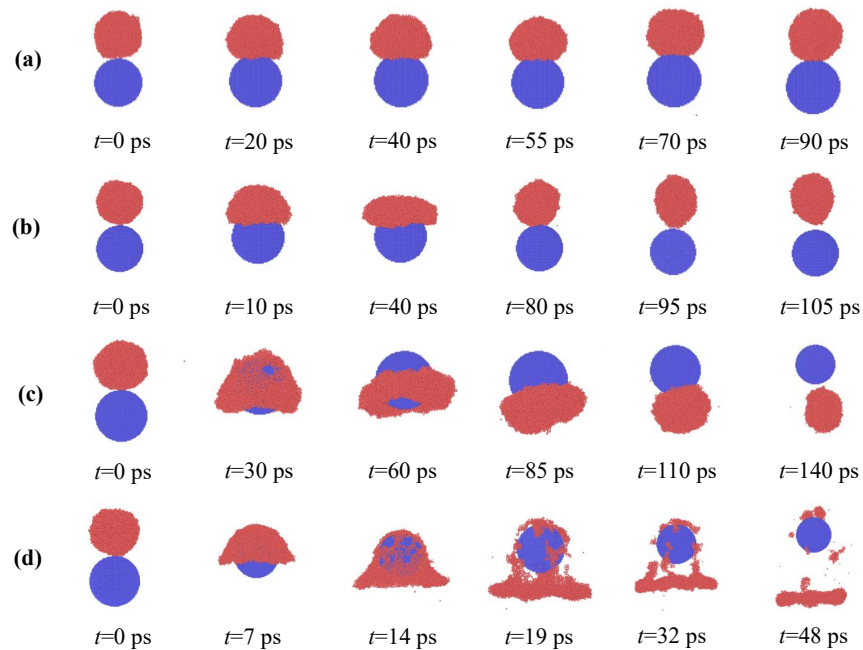

Fig. 7. Temporal evolutions of droplet profiles on the sphere at θ=125° and λ=1 at We = (a) 1.21, (b) 19.32, (c) 59.16, and (d) 146.08.

With the continued increase in impact velocity, the droplet still spreads both longitudinally and

laterally. However, the increased downward kinetic energy causes the crown-shaped liquid film to move downward simultaneously. This leads to stretching of the liquid film at the top of the sphere until a hole appears, followed by the overall downward movement in a ring-shaped manner. Subsequently, the liquid converges and overlaps at the lower end of the sphere to form a spherical droplet, eventually detaching from the sphere to form the dripping 3 state, which is the dripping form previously defined in the literatures[13,48] (Fig. 7c). When the Weber number is very large, the downward movement of the liquid film is rapid, causing the thin liquid film to be quickly torn apart, resulting in the detachment of the liquid film containing more liquid in a conical shape. This process is similar to the formation of dripping 2 on hydrophilic surfaces (Fig. 3d). Therefore, the formation of the dripping 2 state is independent of the surface's hydrophilicity or hydrophobicity and depends only on the Weber number.
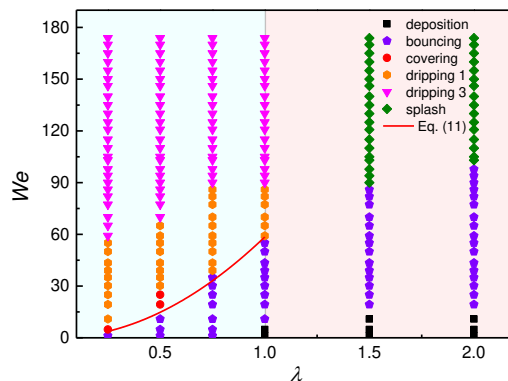

Fig. 8. Phase diagram of nanodroplet impact on a hydrophobic sphere, where We ranges from 1.21 to 173.84 and λ ranges from 0.25 to 2.

In the hydrophobic region, when examining the phase diagram established based on λ and We,

it is noted that the change pattern of droplet impact on a solid sphere in this region is not simply divided by $\lambda=1$, unlike the uniform pattern observed in the hydrophilic region. Instead, it exhibits a more complex and variable outcome, as shown in Fig. 8.

Unlike the hydrophilic region, even within the range of $\lambda \leq 1$, the resulting outcomes of nanodroplet impact on the solid sphere are inconsistent. When $\lambda=0.25$, at very low impact velocities, the droplet initially exhibits a rebound state, similar to an elastic collision. [28,29,59] After impacting the sphere, the droplet only undergoes minor deformation before immediately recoiling and bouncing off. It is important to note that under the same contact angle conditions, there is no rebound phenomenon when a droplet impacts a flat surface.[50] This phenomenon occurs due to the curvature of the sphere, causing the droplet to spread laterally during impact, reducing the contact area between the droplet and the sphere surface, thus minimizing the viscous dissipation.[24] This leads to the occurrence of rebound. Subsequently, with a slight increase in impact velocity, the droplet covers the sphere surface. This is mainly because the solid sphere is relatively small compared with the droplet, so it only requires a small velocity to completely wrap around the sphere. Once covering occurs, the droplet cannot recoil and bounce off the surface anymore. Further increasing the velocity results in the dripping 3 state. This is because the increase in velocity allows the droplet to retain residual kinetic energy even after covering the sphere, leading to continued downward movement. However, the corresponding range of impact velocities for this outcome is significantly larger compared with the previous two outcomes. Finally, under the most impact condition, the droplet exhibits the dripping 2 state, as shown in Fig. 7(d). The transition from dripping 3 to dripping 2 occurs because as the impact velocity increases, the droplet does not return to a spherical shape before detaching from the surface.

Physics of Fluids

When λ=0.50, at relatively low impact velocities, rebound still occurs first, followed by covering. However, the range of impact velocities corresponding to these two outcomes is significantly larger compared with that at λ=0.25. This indicates that as the diameter of the solid sphere increases, the droplet requires a higher velocity to achieve covering of the sphere. Additionally, once covering occurs, more kinetic energy is needed to overcome the energy dissipation generated by the relative motion between the droplet and the larger surface area of the sphere. Similar to the results observed at λ=0.25, under most impact conditions, the droplet exhibits the dripping 2 state.

When λ=0.75, unlike the results for the first two diameter ratios, at this point, due to the relatively close ratio between the sphere diameter and the droplet diameter, when the droplet impacts the sphere at a low velocity, it obtains more spreading space, completely consuming its kinetic energy, and eventually stabilizes at the top of the sphere, forming the deposition state. Moreover, the proportion of rebound states increases significantly, indicating that with the increase in sphere diameter, the maximum spreading diameter of the droplet on the sphere surface increases under the same velocity,[53,60] allowing more surface energy to be stored during the droplet spreading process. The stored surface energy eventually causes the droplet to recoil and bounce off the surface. On the other hand, when λ≥0.75, the covering state no longer occurs after the droplet impacts the sphere. This is because even with an increase in impact velocity, resulting in the droplet covering the sphere, it remains in an unstable state. The thin liquid film formed by the covering is prone to rupture at the top of the sphere due to the presence of residual kinetic energy, and the larger surface energy causes the droplet to contract towards the bottom of the sphere, leading to dripping. Therefore, rebound and dripping represent the two detachment forms of the droplet at the top and

bottom of the sphere, respectively.

At λ=1.00, the impact results are similar to those at λ=0.75. When the droplet impacts the sphere at a low velocity, it initially exhibits the deposition state. As the impact velocity increases, the droplet gains enough energy to rebound from the surface, resulting in a bouncing state. Moreover, the corresponding velocity range for this state further increases. With increasing impact velocity, the dripping 3 and dripping 2 states occur.

However, when λ>1, the impact results under the previous four diameter ratio conditions show significant differences. In this range, at relatively low impact velocities, the droplet still exhibits the deposition state first, followed by rebound. However, the range of impact velocities corresponding to rebound increases significantly. Furthermore, with further increase in impact velocity, similar to the conclusions in the hydrophilic region, the droplet no longer exhibits dripping states but rather splash. Thus, it is once again demonstrated that dripping states only occur when λ≤1, while splash only occurs when λ>1. Taking λ=1.5 and We=10.87, 43.46, 173.85 as examples, the corresponding three states are displayed in Fig. S1 (Supplementary Materials).

Through comparison of the phase diagrams in the hydrophilic and hydrophobic regions, it is observed that the major difference in droplet impact on wetting surfaces lies in the outcomes of rebound, dripping 3, and covering. Due to the enhanced hydrophobicity, at lower velocities, the droplet tends to rebound from the surface after impacting the sphere. Additionally, when λ≤1, within a broad range of velocities, the droplet tends to rupture at the top due to the enhanced hydrophobicity after impacting the sphere, making it unable to maintain the covering morphology. Subsequently, due to insufficient kinetic energy, the droplet contracts into a spherical shape and detaches from the bottom of the sphere, referred to as dripping 3. Furthermore, the covering state in

the hydrophobic region only occupies a very small proportion at λ=0.25 and 0.5, unlike in the hydrophilic region where a large velocity range for covering is observed as long as $\lambda\leqslant1$. This is because the hydrophobic surface exerts a repulsive force on the droplet atoms, making it difficult for the droplet to achieve a stable covering state. Only at smaller λ, where the droplet diameter is significantly larger than the sphere diameter, and at lower velocities, it is possible to achieve complete coverage of the sphere without rupturing the liquid film at the top of the droplet. Therefore, the enhancement of hydrophobicity is the fundamental reason for the differences in these three outcomes. On the other hand, unlike macroscopic droplet impact on hydrophilic spheres, macroscopic droplets impacting hydrophobic spheres typically exhibit rebound behavior, as discussed in detail in the experimental study by Antonini et al.[43]. At the macroscopic scale, droplets on hydrophobic surfaces tend to undergo an expansion-retraction process and may eventually rebound completely off the surface. However, our MD simulations show that at the nanoscale, droplets are more prone to splash or dripping phenomena, especially at higher We. This observation suggests that at the nanoscale, the energy dissipation mechanisms of droplets on hydrophobic surfaces differ from those at the macroscopic scale, resulting in greater fluid instability and the possibility of splashing even at lower critical We.
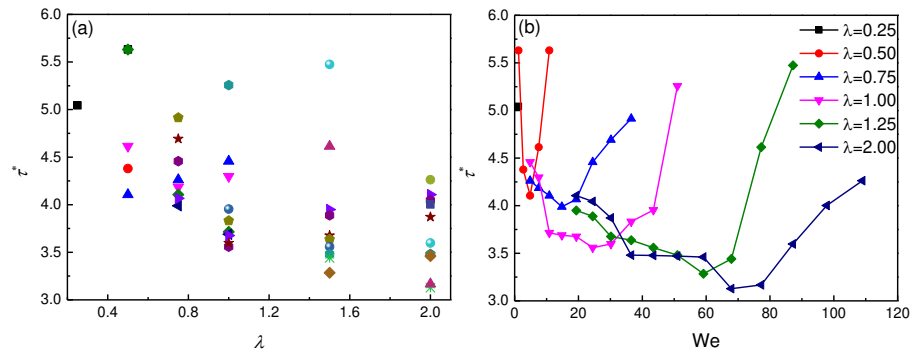
Fig. 9. (a) The relationship between dimensionless contact time τ^* and λ for various We. (b) The relationship between dimensionless contact time τ^* and We for various λ.

Because in applications such as self-cleaning and anti-icing, contact time is the most crucial factor, we summarized the contact time for all rebound cases based on the phase diagram in Fig. 8, and the dimensionless contact time ($\tau^*, \tau^* = \tau/\tau_0$) as a function of λ for distinct We ($1 < We < 110$) is presented in Fig. 9a. At We=1.21 and 4.83, the dimensionless contact time increases with the increase in λ. This is because, at these relatively low impact velocities, the droplet deformation is also small, and the spreading primarily occurs in the lateral direction, similar to impacting on an invisible flat surface (Fig. 7b). Therefore, the increase of λ increases the contact area between the droplet and the wall, thereby enhancing the adhesive effect of the wall on the droplet during the spreading and retracting processes, leading to an increase in contact time. While $We \geq 10.87$, the dimensionless contact time first decreases and then increases as λ increases. As We increases, the deformation of the droplet upon impact also increases, causing it to spread along the spherical surface. Therefore, even if λ slightly increases, it can be considered that there is no effect on the contact area between the droplet and the wall during the spreading process. Here, inertial force is the main factor affecting droplet impact; its increase accelerates the spreading and retracting of the droplet, thereby reducing the contact time. However, with the further increase in λ ($\lambda > 1$), at the top of the sphere, the liquid film is stretched until a hole appears, and under capillary action, the film continues to spread along the sphere, leading to an increase in the hole diameter and eventually forming a ring-shaped liquid film surrounding the solid sphere. Therefore, during the retraction process of this ring-shaped film, it needs to move upward first, overlap at the top of the sphere to form a spherical droplet, and then bounce off the sphere, ultimately resulting in a significant

2

increase in contact time, and the corresponding impacting process can be found in Fig. S2 (Supplementary Materials).

Fig. 9b plots the dimensionless contact time as a function of We for distinct λ. When λ=0.25, rebound occurs only at We=1.21 without a noticeable trend, hence no analysis is conducted. Under all other λ conditions, the dimensionless contact time exhibits a trend of initially decreasing and then increasing. The decrease in contact time is similar to that observed when a droplet impacts a flat surface at low velocities, where the droplet undergoes minimal deformation and behaves akin to an elastic sphere in Hertz contact.[28,29,59] As the impact velocity gradually increases, the degree of droplet deformation increases, deviating from the elastic sphere impact law, and the droplet's higher kinetic energy accelerates both the spreading and retraction processes, thus reducing the rebound time.[12,14,15,60] By comparing the impact processes under different We numbers when $\lambda \leqslant 1$, it is observed that when the droplet achieves the maximum spreading, if the lowest plane of the liquid film does not exceed the center of the solid sphere, the dimensionless contact time gradually decreases with increasing of We. However, when the liquid film continues to spread downward, causing the lowest plane to surpass the center of the solid sphere, the spreading and retraction processes of the droplet consume more time due to a significant increase in viscous dissipation during the impact process. The specific formula can be found in the energy analysis of section 3.3.

When λ>1, the reason for the increased dimensionless contact time at higher We is different from that when $\lambda \leqslant 1$. It is observed that when λ>1, due to the increased diameter of the solid sphere, even at larger We numbers, the spreading's lowest plane cannot exceed the center of the solid sphere. However, with increasing We, the higher downward kinetic energy causes the coronal liquid film in the spreading state to move downward simultaneously. Consequently, a hole appeared at the top of

the sphere, leading to an increase in contact time (Fig. S2).

C. Impact on superhydrophobic sphere

With the increasing maturity of superhydrophobic surface fabrication techniques, the impact behavior of droplets on superhydrophobic surfaces has been widely applied in fields such as self-cleaning, anti-icing, microfluidic systems, biomedical fields.[61-64] Therefore, this paper also delves into the study of the superhydrophobic region. Additionally, we will further explore the differences between macroscopic and nanoscale droplets in several key aspects through quantitative analysis. Specifically, we will further demonstrate the scale effects between the two scales through theoretical models in terms of droplet morphology changes, energy, spreading dynamics, and contact time. It is worth noting that the simulation method used in this study does not explicitly account for the effects of surface microstructures but instead achieves superhydrophobic behavior by adjusting the molecular-level surface wettability. This approach effectively simplifies the calculations while still capturing the main features of surface chemical interactions and has been widely applied in similar studies. In future research, we plan to further investigate the potential impact of microstructures on surface wettability through higher-resolution simulations. In this area, the impact results of droplets are more regular, similar to the hydrophilic region, and can be divided by $\lambda=1$. When $\lambda\leqslant1$, the impact results of droplets on the spherical surface exhibit three outcomes with increasing impact velocity: rebound, dripping 3, and dripping 2. When $\lambda>1$, with increasing impact velocity, droplets first exhibit rebound and then splash. As the various morphologies mentioned above have been elaborately discussed in section 3.2, snapshots are not specifically displayed here. Using $\theta=160°$ as an example, we have established the phase diagram for droplet impact on superhydrophobic solid spheres based on different λ and We numbers, as illustrated in Fig.

10. However, on superhydrophobic surfaces, the experimental study by Liu et al.[65] shows that droplets tend to exhibit complete rebound, with little to no residual on the surface. Our MD simulation results support this observation; however, at the nanoscale, the rebound behavior of droplets on superhydrophobic surfaces may exhibit higher sensitivity. For example, within specific Weber number ranges, droplets may not rebound as smoothly as in macroscopic experiments but may instead undergo asymmetric rebound or even splashing. This further demonstrates that at the nanoscale, due to surface effects and the high kinetic energy of molecules within the droplet, the rebound behavior becomes more complex.
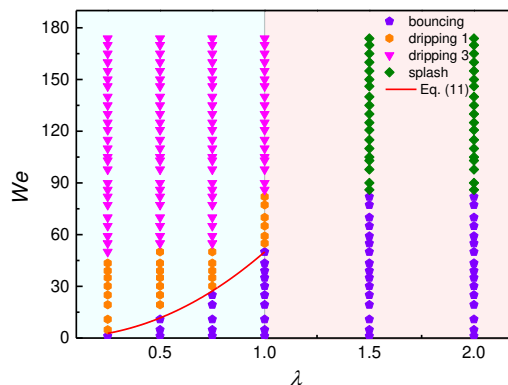

Fig. 10. Phase diagram of nanodroplet impact on a superhydrophobic sphere, where We ranges from 1.21 to 173.84 and λ ranges from 0.25 to 2.

After comparing the phase diagram results of the hydrophilic and hydrophobic regions, it is evident that on superhydrophobic surfaces, due to the excessive hydrophobicity, droplets do not stay on the sphere. Thus, deposition or covering does not occur, only rebound from the top of the sphere and dripping from the bottom are observed when $\lambda \leqslant 1$. Therefore, only two forms of detachment

states of droplets on superhydrophobic surfaces are generated. Consequently, based on the principle of energy conservation, we established a theoretical model to quantitatively predict the critical transition conditions between the outcomes of rebound and dripping.

Based on the snapshots of the droplet impact process in Fig. 7, the impact droplet forms a crown-shaped structure. Generally, if there is still surplus kinetic energy to continue spreading after the plane at the bottom end of the crown-shaped liquid film surpasses the bottom vertex of the solid sphere, dripping occurs. Conversely, if the plane at the bottom end of the crown-shaped liquid film remains above the sphere before reaching maximum expansion, rebound occurs. Therefore, it is assumed that there exists a critical state between droplet rebound and dripping. In this state, the droplet has reached maximum expansion without any surplus energy. The initial and critical states of the droplet impact are illustrated in Fig. 11.

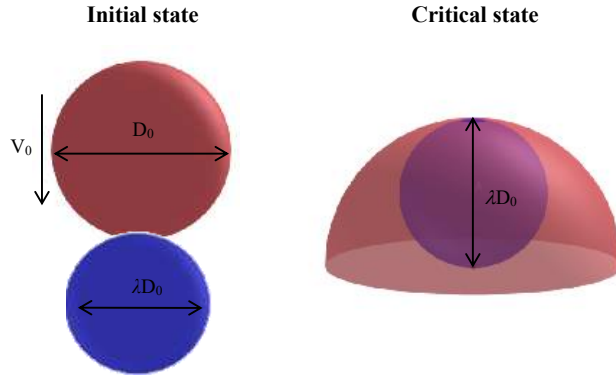**Initial state** **Critical state**

Fig. 11. Schematics of the initial state and critical state for the transition from rebound to dripping regimes, where the impacting droplet forms a crown shape surrounding the sphere in the critical state.

During the impact process, the energy expressions for the two states satisfy the equation:

$$E_{k,0} + E_{s,0} = E_k + E_s + E_{vis} \qquad (2)$$

where $E_{k,0}$ and $E_{s,0}$ are the initial kinetic energy and surface energy; E_k and E_s are the critical kinetic energy and surface energy; and E_{vis} is the viscous dissipation. The energy terms at the initial state can be obtained from

$$E_{k,0} = \frac{\pi}{12} \rho D_0^3 V_0^2 \qquad (3)$$

$$E_{s,0} = \gamma_{gl} A_{gl,0} + \gamma_{gs} A_{gs,0} = \gamma_{gl} \cdot \pi D_0^2 + \gamma_{gs} \cdot \pi (\lambda D_0)^2 \qquad (4)$$

where γ_{gl} and γ_{gs} are the gas–liquid and gas–solid surface tensions, respectively; $A_{gl,0}$ and $A_{gs,0}$ are the surface area of the initial droplet and solid sphere. Upon reaching the critical state (Fig. 11), the droplet's kinetic energy usually accounts for less than 5% of the initial total energy at maximum spreading.[76] Consequently, the energy components become.

$$E_k \approx 0 \qquad (5)$$
$$E_s = \gamma_{gl} A_{gl} + \gamma_{sl} A_{sl} \qquad (6)$$

where γ_{ls} is the liquid-solid surface tension and is connected to γ_{gl} and γ_{gs} through Young's equation, namely,

$$\gamma_{gl} \cos\theta_Y = \gamma_{gs} - \gamma_{ls} \qquad (7)$$

where θ_Y is taken to be the static contact angle (θ). It is worth noting that Young's equation was used within this theoretical framework. Although Young's equation was originally proposed for macroscopic scales, recent research has shown that it remains applicable under specific nanoscale conditions, such as when the surface is sufficiently smooth, the droplet size is relatively large, and the system is somewhat idealized.[67,68] Therefore, in our study, where the system meets these specific conditions, Young's equation remains a reasonable and useful tool. Because the solid sphere is completely enveloped by the droplet, the surface energy at the critical state consists of two parts: the gas-liquid interface area of the spherical droplet and the solid-liquid interface area where it contacts the solid sphere. The calculation results are as follows:

$$A_{gl} = \frac{2 + 3\lambda^3}{3\lambda}\pi D_0^2 \qquad (8)$$

$$A_{sl} = \pi(\lambda D_0)^2 \qquad (9)$$

Unlike macroscopic droplet impacts, at this scale, the calculation of viscous dissipation only considers the boundary layer. As we move to the nanoscale, velocity gradients exist throughout the entire droplet.[32,34,48] Therefore, the calculation formula can refer to the method proposed by Mao,[37] where viscous dissipation includes both the boundary layer and the interior of the droplet, expressed as:

$$E_{vis} \approx \frac{1}{2}\pi D_0^2 \gamma_{gl} \frac{We}{Re}\left(\frac{L_{w,\max}}{D_0}\right)^4 = \frac{2\pi^3 \gamma_{gl} We}{9\lambda^2 D_0^2 Re} \qquad (10)$$

By substituting equations (3)-(10) into equation (2), we obtain the critical condition for the rebound and dripping outcomes of impact droplets on small superhydrophobic spheres, i.e.,

$$We + 12\left(1 - \frac{2 + 3\lambda^3}{3\lambda} - \lambda^2\cos\theta\right) - \frac{8\pi^2 We}{3\lambda^2 D_0^4 Re} = 0 \qquad (11)$$

As anticipated, the critical curves derived from the theoretical model [Eq. (11)] effectively matches the transition between the rebound and dripping outcomes when $\lambda \leq 1$, as depicted in Figs. 8 and 10. As the diameter ratio increases, the critical Weber numbers for the transition between rebound and dripping, as determined by both simulations and the theoretical model, also increase, and closely align. Despite a slight deviation at some diameter ratios, it might stem from the assumption about the critical state, such as simplifying the shape of the deformed droplet, or estimating viscous dissipation. Given the complexity of fluid flow during droplet impact, this deviation is acceptable and indicates that the theoretical model can reliably predict the final outcome of a droplet impacting a small superhydrophobic sphere. It should be noted that Liu et al.[13] also established a theoretical boundary between the rebound and dripping states using the energy conservation method. However, their geometric model and energy dissipation were proposed based

3

on a macroscopic scale, which does not correspond with our microscopic results, as demonstrated in the study by Wang et al.[48]. However, in Wang's research on the impact of nano-droplets on a sphere, the theoretical model derived is based on the proportionality between the difference in surface energy and the difference in kinetic energy.[48] This is only applicable to the range where the coefficient of restitution does not change with the Weber number, meaning the rebound time does not vary with the Weber number.[32,50] However, as shown in Fig. 12b, during the transition from the rebound state to the dripping state, the rebound time no longer falls within the range where it is independent of the Weber number. Therefore, this theoretical model does not accurately reflect the real energy relationship at the critical state.

Whether it is a droplet impact on a superhydrophobic flat surface or a spherical surface, the phenomenon of rebound is the most crucial outcome. Therefore, we extracted the dimensionless contact time of the rebound cases from Fig. 10 and analyzed them, as shown in Fig. 12. In Fig. 12a, when $1.21 \leq We \leq 10.87$, the dimensionless contact time first decreases and then increases with the increase in λ. This is significantly different from the trend observed on hydrophobic surfaces (Fig. 8a), but the reason for the increase in contact time is the same: the increase in the contact area between the droplet and the wall. The initial decreasing trend is due to the enhanced hydrophobicity, causing the droplet to spread mainly in the horizontal direction upon impact. Therefore, a smaller λ does not affect the contact area, and the contact time is determined solely by the inertial force. When $19.32 \leq We \leq 43.46$, the dimensionless contact time first decreases and then remains unchanged with the increase in λ. The reason for the decreasing trend in contact time is that the smaller the λ, the more pronounced the curvature effect becomes. Specifically, when λ is smaller, the spreading of the droplet is significantly influenced by the curvature, leading to a greater extent of wrapping and

spreading. Therefore, the entire spreading and retraction process takes longer. However, as λ increases, the degree of spreading stabilizes and becomes more consistent, the curvature effect gradually diminishes or even disappears, and the contact time tends to remain constant. At $We \geq 59.16$, the dimensionless contact time decreases with the increase in λ. At this point, a hole appears at the top of the liquid film in all impact processes, and the influence of curvature disappears. Inertial force becomes the dominant force affecting the contact time. Therefore, the greater the impact velocity, the shorter the contact time is.
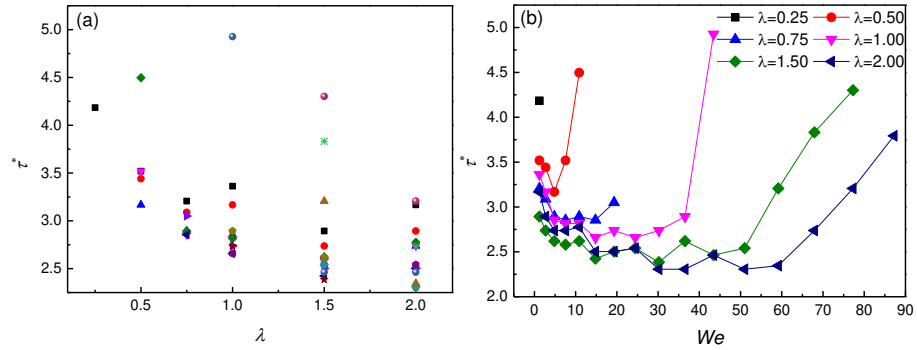

Fig. 12. (a) The relationship between dimensionless contact time τ^* and λ for various We. (b) The relationship between dimensionless contact time τ^* and We for various λ.

In Fig. 12b, when $\lambda=0.25$, similar to the results on the hydrophobic spherical surface in Section 3.2, rebound only occurs at $We=1.21$. This indicates that under such extremely small diameter ratios, whether on a hydrophobic or superhydrophobic surface, only at low velocities will there be a rebound similar to that of an elastic sphere. As the impact velocity increases slightly, the post impact morphology changes. For the rest of the diameter ratio conditions, the contact time initially decreases and then increases, which is consistent with the rebound time pattern on a hydrophobic sphere. The reason for this trend is also unified and can be found in detail in Section 3.2.

Unlike the impact of droplets on a hydrophobic sphere, in the mid-Weber number range, the contact time exhibits a generally constant trend, which is similar to droplets impacting on a superhydrophobic flat surface.[32] It was proposed for the first time in their study that, during the impact of nanoscale droplets, the contact time no longer follows macroscopic laws. It is not only related to the Weber number but also to the Reynolds number. Their work quantitatively demonstrated the key role of viscous in the impact process of nanoscale droplets, proposing that the contact time $t \sim (R_0/V_0)We^{2/3}Re^{-1/3}$. Subsequently, Wang et al.[34] and Ma et al.[69] derived that the maximum spreading factor and the rebound time on surfaces with different wettabilities were both proportional to $We^{2/3}Re^{-1/3}$. Therefore, the contact time on solid spheres is needed to be established by extending the effectiveness of this scaling law from flat surfaces to solid spheres.

To extend the scaling relationship of contact time for nanoscale droplet impacts from flat surfaces to spherical surfaces, an important influencing factor, λ, must be considered. Therefore, for droplet impacts on cylinders at the macroscale, a revised Weber number is introduced to account for the interplay between inertia and capillarity on curved surfaces, expressed as $We^*=We/\lambda$.[70-72] Similarly, a revised Reynolds number can be expressed as $Re^*=Re/\lambda$. Thus, the new revised scaling relationship can be expressed as $t \sim (D_0/V_0)We^{2/3}Re^{-1/3}\lambda^{-1/3}$. To verify this scaling, four more sets of simulations were carried out at λ=0.75, 1.00, 1.50, and 2.00, using impact velocities that fall within the constant contact time region for these radius ratio conditions. We define a revised dimensionless time as $t^*=t/(D_0/V_0)$ and plot all data in a $t^* \sim We^{2/3}Re^{-1/3}\lambda^{-1/3}$ coordinate system. Intriguingly, all four sets of data collapse onto a single universal curve, as shown in Fig. 13, thereby verifying this scaling.
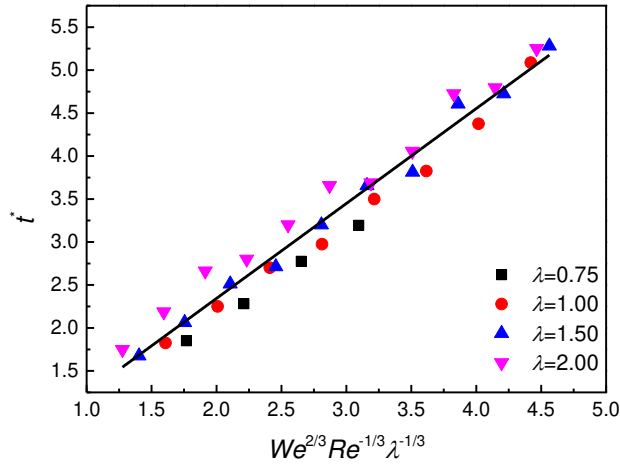
Fig. 13. Revised dimensionless contact time t^* as a function of $We^{2/3}Re^{-1/3}\lambda^{-1/3}$ for various λ,

fitted with a power-law $t^* \sim We^{2/3}Re^{-1/3}\lambda^{-1/3}$.

IV. CONCLUSION

This study investigates the impact dynamics of nanodroplet on solid spheres, using the MD simulations. The simulations explored a wide parametric range with We from 1.2 to 173.8, λ from 0.25 to 2, and θ from 21° to 160°, aiming to reveal a detailed understanding of the impact dynamics and comprehensively report the outcome regimes. When a droplet impacts on a hydrophilic sphere, five impact outcomes are observed: deposition, covering, ligament-structured dripping, conical-structured dripping, and splash. Moreover, $\lambda=1$ can be regarded as the boundary dividing the impact outcomes into a complex region with smaller λ values ($\lambda \leqslant 1$) and a relatively simple region similar to droplet impacts on flat surfaces with larger λ values ($\lambda > 1$). Dripping states only occur when $\lambda \leqslant 1$, while splash only occurs when $\lambda > 1$. When a droplet impacts on a hydrophobic sphere, six impact outcomes are observed: deposition, rebound, covering, dripping,

3

conical-structured dripping, and splash. Due to enhanced hydrophobicity, compared with impacts on hydrophilic spheres, rebound and dripping outcomes emerge, while ligament-structured dripping no longer occurs. Additionally, the proportion of covering outcomes decreases significantly. Furthermore, we calculated the contact time for all rebound cases and found that under all λ conditions, as Weber number increases, the contact time initially decreases and then increases. This is mainly attributed to different spreading and recoiling behaviors during droplet impact, resulting in varying viscous dissipation. When a droplet impacts on a superhydrophobic sphere, the impact outcomes are more regular. Similar to the hydrophilic region, $\lambda=1$ can also serve as a boundary, when $\lambda \leqslant 1$, deposition, dripping, and conical-structured dripping are observed, while when $\lambda>1$, only rebound and splash are observed.

An energy analysis of impacts on superhydrophobic solid spheres was carried out to systematically explore the effects of λ and We on rebound and dripping criteria. A theoretical model correlating We, θ, and λ has been established and the findings in this study demonstrate that the criteria for rebound and dripping can be effectively predicted using this theoretical model, which takes into account surface curvature and wettability. Furthermore the rebound time of droplet impact on superhydrophobic spherical surfaces has been investigated. By introducing the modified Weber (We/λ) and Reynolds (Re/λ) numbers, we extended the scaling law of contact time previously established for droplet impact on superhydrophobic flat surfaces to spherical surfaces. The new scaling relationship is $t^* \sim (D_0/V_0)We^{2/3}Re^{-1/3}\lambda^{-1/3}$, which agrees well with the simulated results. The findings in this study enhance the understanding of droplet impact on solid spheres, contributing significantly to the control of impact dynamics in applications like painting, spray cooling, coating, 3D printing, drug delivery, and various other fields.

SUPPLEMENTARY MATERIAL

See the supplementary material for details on the nanodroplets impacting a hydrophobic surface (S1), and the impact and rebound process of a nanodroplet with a hole (S2).

ACKNOWLEDGMENTS

AUTHOR DECLARATIONS

Conflict of Interest

The authors have no conflicts to disclose.

AUTHOR CONTRIBUTIONS

Mingjun Liao: Investigation, Writing – original draft, Methodology, Conceptualization. **Qianyi Liu**: Writing – original draft, Visualization, Formal analysis, Data curation. **Zhiyin Yang**: Writing – review & editing. **Amirali Shateri**: Writing – review & editing. **Wenpeng Hong**: Writing – review & editing. **Fangfang Xie**: Writing – review & editing, Supervision, Funding acquisition, Project administration.

DATA AVAILABILITY

Data will be made available on request.

REFERENCES

[1] M. Garbero, M. Vanni, and G. Baldi, "CFD modelling of a spray deposition process of paint," Macromol Symp **187**, 719-730 (2002).

[2] J. Kim, "Spray cooling heat transfer: The state of the art," Int. J. Heat Fluid Flow **28**, 753767 (2007).

[3] D. A. Bolleddula, A. Berchielli, and A. Aliseda, "Impact of a heterogeneous liquid droplet on a dry surface: application to the pharmaceutical industry," Adv. Colloid Interface Sci. **159**, 14459

(2010).

4   J.Y. Lee, J. An, and C. K. Chua, "Fundamentals and applications of 3D printing for novel materials," Appl. Mater. Today **7**, 120133 (2017).

5   D. Khojasteh, N. M. Kazerooni, and M. Marengo, "A review of liquid droplet impacting onto solid spherical particles: A physical pathway to encapsulation mechanisms," J Ind Eng Chem **71**, 5064 (2019).

6   Y. Wang, "Numerical study of a droplet impact on cylindrical objects: Towards the anti-icing property of power transmission lines," Appl. Surf. Sci **16**, 146155 (2020).

7   R. P. Patel, M. P. Patel, and A. M. Suthar, "Spray drying technology: an overview," Indian J Sci Technol **2**, 4447 (2009).

8   I. Malgarinos, N. Nikolopoulos, and M. Gavaises, "Numerical investigation of heavy fuel droplet-particle collisions in the injection zone of a Fluid Catalytic Cracking reactor, Part I: Numerical model and 2D simulations," Fuel Process Technol **156**, 317330 (2017).

9   S. A. Banitabaei, and A. Amirfazli, "Droplet impact onto a solid sphere: Effect of wettability and impact velocity," Phys. Fluids **29**, 062111 (2017).

10   X. X. Li, Y. C. Fu, D. Zheng, Y. H. Fang, and Y. X. Wang, "A numerical study of droplet impact on solid spheres: The effect of surface wettability, sphere size, and initial impact velocity," Chem. Phys **550**, 111314 (2021).

11   Y. X. Du, J. Liu, Y. Z. Li, J. Y. Du, X. X. Wu, and Q. Min, "Numerical study on droplets impacting solid spheres: Effect of fluid properties and sphere diameter," Colloid Surfaces A **625**, 126862 (2021).

12   L. Xia, F. Z. Chen, Z. Yang, T. Liu, Y. L. Tian, and D. W. Zhang, "Droplet impact dynamics on superhydrophobic surfaces with convex hemispherical shapes," Int. J. Mech Sci **264**, 108824 (2024).

13   X. Liu, X. Zhang, and J. C. Min, "Droplet rebound and dripping during impact on small superhydrophobic spheres," Phys. Fluids **34**, 032118 (2022).

14   X. X. Li, H. W. Li, D. Zheng, and Y. X. Wang, "Many-body dissipative particle dynamics study of droplet impact on superhydrophobic spheres with different size," Colloid Surfaces A **618**, 126493 (2021).

15   H. N. Dalgamoni, and X. Yong, "Numerical and theoretical modeling of droplet impact on

spherical surfaces," Phys. Fluids **33**, 052112 (2021).

[16] M. Benz, A. Asperger, M. Hamester, A. Welle, S. Heissler, and P. A. Levkin, "A combined high-throughput and high-content platform for unified on-chip synthesis, characterization and biological screening," Nat. Commun **11**, 5391 (2020).

[17] A. Ishijima, K. Minamihata, S. Yamaguchi, S. Yamahira, R. Ichikawa, E. Kobayashi, M. Iijima, Y. Shibasaki, T. Azuma, and T. Nagamune, "Selective intracellular vaporisation of antibody-conjugated phase-change nano-droplets in vitro," Sci. Rep **7**, 44077 (2017).

[18] M. W. Glasscott, A. D. Pendergast, S. Goines, A. R. Bishop, A. T. Hoang, C. Renault, and J. E. Dick, "Electrosynthesis of high-entropy metallic glass nanoparticles for designer, multi-functional electrocatalysis," Nat. Commun **10**, 2650 (2019).

[19] F. Liu, G. Ghigliotti, J. J. Feng, and C. H. Chen, "Numerical simulations of self-propelled jumping upon drop coalescence on nonwetting surfaces," J. Fluid Mech. **752**, 3965 (2014).

[20] T. Kondo, and K. Ando, "Simulation of high-speed droplet impact against a dry/wet rigid wall for understanding the mechanism of liquid jet cleaning," Phys. Fluids **31**, 013303 (2019).

[21] J. Eggers, M. A. Fontelos, C. Josserand, and S. Zaleski, "Drop dynamics after impact on a solid wall: Theory and simulations," Phys. Fluids **22**, 062101 (2010).

[22] Z. Liang, and P. Keblinski, "Coalescence-induced jumping of nanoscale droplets on super-hydrophobic surfaces," Appl. Phys. Lett **107**, 143105 (2015).

[23] F. F. Xie, G. Lu, X. D. Wang, and B. B. Wang, "Coalescenceinduced jumping of two unequal-sized nanodroplets," Langmuir **34**, 27342740 (2018).

[24] F. F. Xie, G. Lu, X. D. Wang, and D. Q. Wang, "Enhancement of coalescence-induced nanodroplet jumping on superhydrophobic surfaces," Langmuir **34**, 11195 (2018).

[25] S. Arora, J. M. Fromental, S. Mora, T. Phou, L. Ramos, and C. Ligoure, "Impact of beads and drops on a repellent solid surface: a unified description," Phys. Rev. Lett **120**, 148003 (2018).

[26] V. Zorba, E. Stratakis, M. Barberoglou, E. Spanakis, P. Tzanetakis, S. H. Anastasiadis, and C. Fotakis, "Biomimetic artificial surfaces quantitatively reproduce the water repellency of a lotus leaf," Adv. Mater **20**, 40494054 (2008).

[27] K. Okumura, F. Chevy, D. Richard, D. Quere, and C. Clanet, "Water spring: A model for bouncing drops," Europhys Lett **62**, 237243 (2003).

[28] Y. Tanaka, Y. Yamazaki, and K. Okumura, "Bouncing gel balls: Impact of soft gels onto rigid

surface," Europhys Lett **63**, 146152 (2003).

[29] D. Bartolo, F. Bouamrirene, E. Verneuil, A. Buguin, P. Silberzan, and S. Moulinet, "Bouncing or sticky droplets: Impalement transitions on superhydrophobic micropatterned surfaces," Europhys Lett **74**, 299305 (2006).

[30] Tsai, P. Pacheco, S. Pirat, C. Lefferts, and L. Lohse, "Drop impact upon micro-and nanostructured superhydrophobic surfaces," Langmuir **25**, 12293 (2009).

[31] J. C. Bird, J. Dhiman, H. M. Kwon, and K. K. Varanasi, "Reducing the contact time of a bouncing drop," Nature **503**, 385388 (2013).

[32] F. F. Xie, S. H. Lv, Y. R. Yang, and X. D. Wang, "Contact time of a bouncing nanodroplet," J. Phys. Chem. Lett **11**, 2818 (2020).

[33] C. Clanet, C. Beguin, D. Richard, and D. Quéré, "Maximal deformation of an impacting drop," J. Fluid Mech **517**, 199 (2004).

[34] Y. F. Wang, Y. B. Wang, X. He, B. X. Zhang, Y. R. Yang, X. D. Wang, and D. J. Lee, "Scaling laws of the maximum spreading factor for impact of nanodroplets on solid surfaces," J. Fluid Mech **937**, A12 (2022).

[35] J. B. Lee, D. Derome, A. Dolatabadi, and J. Carmeliet, "Energy budget of liquid drop impact at maximum spreading: Numerical simulations and experiments," Langmuir **32**, 1279 (2016).

[36] J. B. Lee, D. Derome, R. Guyer, and J. Carmeliet, "Modeling the maximum spreading of liquid droplets impacting wetting and nonwetting surfaces," Langmuir **32**, 1299 (2016).

[37] T. Mao, D. C. Kuhn, and H. Tran, "Spread and rebound of liquid droplets upon impact on flat surfaces," AIChE J **43**, 2169 (1997).

[38] M. P. Fard, Y. Qiao, S. Chandra, and J. Mostaghimi, "Capillary effects during droplet impact on a solid surface," Phys. Fluids **8**, 650 (1996) .

[39] C. W. Visser, P. E. Frommhold, S. Wildeman, R. Mettin, D. Lohse, and C. Sun, "Dynamics of high-speed micro-drop impact: Numerical simulations and experiments at frame-to-frame times below 100 ns," Soft Matter **11**, 1708 (2015).

[40] C. W. Visser, Y. Tagawa, C. Sun, and D. Lohse, "Microdroplet impact at very high velocity," Soft Matter **8**, 10732 (2012).

[41] S. Wildeman, C. W. Visser, C. Sun, and D. Lohse, "On the spreading of impacting drops," J. Fluid Mech **805**, 636655 (2016).

4

[42] C. Antonini, A. Amirfazli, and M. Marengo, "Drop impact and wettability: From hydrophilic to superhydrophobic surfaces," Phys. Fluids **24**, 102104 (2012).

[43] T. Gilet, and J. W. M. Bush, "Droplets bouncing on a wet, inclined surface," Phys. Fluids **24**, 122103 (2012).

[44] H. M. Huang, and X. P. Chen, "Energetic analysis of drop's maximum spreading on solid surface with low impact speed," Phys. Fluids **30**, 022106 (2018).

[45] X. H. Li, X. X. Zhang, and M. Chen, "Estimation of viscous dissipation in nanodroplet impact and spreading," Phys. Fluids **27**, 052007 (2015).

[46] Z. J. Yin, Z. L. Ding, X. G. Ma, X. P. Zhang, and Y. Xia, "Molecular Dynamics Simulations of Single Water Nanodroplet Impinging Vertically on Curved Copper Substrate," Microgravity Sci Tec **31**, 749-757 (2019).

[47] L. X. Zhan, H. Chen, H. Zhou, J. W. Chen, H. Wu, and L. J. Yang, "Droplet-particle collision dynamics: A molecular dynamics simulation," Powder Technol. **422,** 118456 (2023).

[48] Y. F. Wang, Q. Ma, B. J. Wei, S.R. Gao, Y. R. Yang, S. F Zheng, D. J. Lee, and X. D. Wang, "Impact of nanodroplets on solid spheres," Phys. Fluids **35**, 2082118 (2023).

[49] V. Molinero, and E. B. Moore, "Water modeled as an intermediate element between carbon and silicon," J. Phys. Chem. B **113**, 4008-4016 (2009).

[50] Q. Ma, Y. F. Wang, Y. B. Wang, X. He, S. F. Zheng, Y. R. Yang, X. D. Wang, and D. J. Lee, "Phase diagram for nanodroplet impact on solid surfaces," Phys. Fluids **33**, 102007 (2021).

[51] A. Stukowski, "Visualization and analysis of atomistic simulation data with OVITO the open visualization tool," Model. Simul Mater Sci Eng **18**, 015012 (2010).

[52] B. X. Li, X. H. Li, and M. Chen, "Spreading and breakup of nanodroplet impinging on surface," Phys. Fluids **29**, 012003 (2017).

[53] Y. F. Wang, Y. B. Wang, F. F. Xie, J. Y. Liu, S. L. Wang, Y. R. Yang, S. R. Gao, and X. D. Wang, "Spreading and retraction kinetics for impact of nanodroplets on hydrophobic surfaces," Phys. Fluids **35**, 092005 (2020).

[54] I. Yoon, and S. Shin, "Direct numerical simulation of droplet collision with stationary spherical particle: a comprehensive map of outcomes," Int J Multiphase Flow **135**, 103503 (2021).

[55] J. Palacios, J. Hernández, P. Gómez, C. Zanzi, and J. López, "Experimental study of splashing patterns and the splashing/deposition threshold in drop impacts onto dry smooth solid surfaces,"

Exp Therm Fluid Sci **44**, 571–582 (2013).

[56] I. Bischofberger, K. W. Mauser, and S. R. Nagel, "Seeing the invisible-air vortices around a splashing drop," Phys. Fluids **25**, 09111 (2013).

[57] Y. B. Wang, Y. F. Wang, X. Wang, B. X. Zhang, Y. R. Yang, D. J. Li, X. D. Wang, and M. Chen, "Splash of impacting nanodroplets on solid surfaces," Phys. Rev. Fluids **6**, 094201 (2021).

[58] R. Rioboo, M. Marengo, and C. Tropea, "Time evolution of liquid drop impact onto solid, dry surfaces," Exp Fluids **33**, 112-124 (2002).

[59] D. Richard, C. Clanet, and D. Quéré, "Contact time of a bouncing drop," Nature **417**, 811-811 (2002).

[60] J. Han, W. Kim, C. Bae, D. Lee, S. Shin, Y. Nam, and C. Lee, "Contact time on curved superhydrophobic surfaces," Phys Rev E **101**, 043108 (2020).

[61] L. Feng, M. Yang, X. Shi, Y. Liu, Y. Wang, and X. Qiang, "Copper-based superhydrophobic materials with long-term durability, stability, regenerability, and self-cleaning property," Colloid Surfaces A **508**, 39–47 (2016).

[62] N. Wang, D. Xiong, Y. Deng, Y. Shi, and K. Wang, "Mechanically robust superhydrophobic steel surface with anti-icing, UV-durability, and corrosion resistance properties," ACS Appl. Mater. Inter **7**,6260–6272 (2015).

[63] J. Chao, J. Feng, F. Chen, B. Wang, Y. Tian, and D. Zhang, "Fabrication of superamphiphobic surfaces with controllable oil adhesion in air," Colloids Surf Physicochem Eng Asp **610**, 125708 (2021).

[64] N. J. Shirtcliffe, G. McHale, M. I. Newton, Y. Zhang, "Superhydrophobic copper tubes with possible flow enhancement and drag reduction," ACS Appl Mater Inter **1**, 1316–1323 (2009).

[65] Y. Liu, L. Moevius, X. Xu, T. Qian, J. M. Yeomans, and Z. Wang, "Pancake bouncing on superhydrophobic surfaces," Nat. Phys **10**, 515-519 (2014).

[66] X. Zhang, B. Ji, X. Liu, S. Ding, X. Wu, and J. Min, "Maximum spreading and energy analysis of ellipsoidal impact droplets," Phys. Fluids **33**, 052108 (2021).

[67] Z. Luo, and X. Zhuang, "Validity of Young's equation at the nanoscale: Insights from molecular dynamics simulations," J Chem Phys **148**, 024701 (2018).

[68] J. Wang, and H. Liu, "Young's equation and nanoscale wetting: A molecular dynamics perspective," Phys. Chem. Chem. Phys **21**, 6508-6516 (2019).

4

[69] Q. Ma, Y. F Wang, Y. B. Wang, B. X. Zhang, S. F. Zheng, T. R. Yang, D. J. Lee, and X. D. Wang, "Scaling laws for the contact time of impacting nanodroplets: From hydrophobic to superhydrophobic surfaces," Phys. Fluids **35**, 062003 (2023).

[70] H. Zhang, X. Yi, Y. Du, R. Zhang, X. Zhang, F. He, F. Niu, and P. Hao, "Dynamic behavior of water drops impacting on cylindrical superhydrophobic surfaces," Phys. Fluids **31**, 032104 (2019).

[71] É. Lorenceau, C. Clanet, and D. Quéré, "Capturing drops with a thin fiber," J Colloid Interface Sci **279**, 192–197 (2004).

[72] S. G. Kim, and W. Kim, "Drop impact on a fiber," Phys. Fluids **28**, 042001 (2016).